Evolution of the Domain Topology in a Ferroelectric

S. C. Chae, Y. Horibe, D. Y. Jeong, N. Lee, K. Iida, M. Tanimura, and S.-W. Cheong

Phys. Rev. Lett. **110**, 167601 — Published 15 April 2013

DOI: 10.1103/PhysRevLett.110.167601

Evolution of the domain topology in a ferroelectric

S. C. Chae[1], Y. Horibe[1], D. Y. Jeong[2], N. Lee[1], K. Iida[3], M. Tanimura[3] and S.-W. Cheong[1*]

[1]Rutgers Center for Emergent Materials and Department of Physics and Astronomy, Rutgers, The State University of New Jersey, Piscataway, NJ 08854

[2]Department of Mathematics, Soongsil University, Seoul 156-743, Korea

[3]Research Department, Nissan Arc, Ltd., Yokosuka, Kanagawa 237-0061, Japan

[*]e-mail: sangc@physics.rutgers.edu

Topological materials, including topological insulators, magnets with skyrmions and ferroelectrics with topological vortices, have recently attracted phenomenal attention in the materials science community. Complex patterns of ferroelectric domains in hexagonal $REMnO_3$ (RE: rare earths) turn out to be associated with the macroscopic emergence of $Z_2 \times Z_3$ symmetry. The results of our depth profiling of crystals with self-poling tendency near surfaces reveal that the partial dislocation (i.e., wall-wall) interaction, not the interaction between vortices and antivortices, is primarily responsible for topological condensation through the macroscopic breaking of the Z_2-symmetry.

Symmetries govern nature ubiquitously from the beauty of human faces [1] to the local gauge invariance of quantum field theory [2]. The spontaneous breaking of symmetry by a variable such as temperature gives rise to a phase transition. Dislocations are common topological defects in materials, which occur during symmetry breaking, and often effectively determine important fundamental crystal properties such as hardness and fatigue behavior, grain boundary development, and charge density wave discommensuration [3-5]. The Burgers vector characterizes each dislocation, and dislocation and anti-dislocation refer to two dislocations with oppositely directed Burgers vectors. Dislocations with Burgers vectors that are not translation vectors with integer times of the underlying lattice unit are called partial dislocations. For example, a charge density wave (CDW) discommensuration can be considered as a partial dislocation with a Burgers vector that is a fraction of a unit cell vector and a few of these discommensulations terminate at a full "CDW dislocation", corresponding to a topological defect with a unit-cell Burgers vector [6, 7]. Dislocations can often interact with each other like particles in a dilute gas [8]. The overlap between the strain fields of adjacent dislocations can induce a paired interaction between the dislocations.

Ferroelectric hexagonal-$REMnO_3$ (RE: rare earths) exhibit intriguing topological defects induced through a trimerization-type structural phase transition [9-12]. This structural transition leads to three structural antiphase domains (α, β, γ), each of which can support either of two directions (+,–) of ferroelectric polarization [13, 14]. The six interlocked structural antiphase and ferroelectric domains of $REMnO_3$ meet in a cloverleaf arrangement that cycles through all six domain configurations [15, 16]. Occurring in pairs, the cloverleaves can be viewed as vortices and antivortices with opposite cycle of domain configuration. We have observed two topologically-distinct types of large-scale vortex/antivortex domain patterns; type-I without any preferred polarization direction, and type-II with a preferred polarization direction [17]. However, the physical nature of switching between type-I to type-II patterns has not been understood.

Herein, we report depth profiling of the ferroelectric domain patterns in two hexagonal $ErMnO_3$ crystal and the symmetry change of the patterns with increasing depth. We have prepared one crystal (EMO-A) with upward polarization favored near the top a-b surfaces and the other crystal (EMO-B) with the opposite tendency (see the detailed experimental methods in the Supplementary Information). The evolution of ferroelectric domain configurations along the c axis was investigated by sequential selective chemical etching and taking optical microscope and atomic force microscope (AFM) images of both of the a-b surfaces of EMO-A. Cross-sectional TEM experiments were performed on EMO-B. Note that the evolution of the domain pattern with increasing depth is not due to the increasing degree of chemical etching and the as discussed in the Supplementary Information section 1.

We have found that the ferroelectric domain configurations at both of the original surfaces of the EMO-A sample were type-II, but became type-I in the interior of the crystal as shown in Fig. 1 (and Fig. S2 in the Supplementary Information section 2). Note that the two parallel surfaces of the crystal favor opposite polarization domains as shown schematically in Fig. S2(e) and S2(h). The differential chemical etching between upward and downward polarization domains resulted in etched surfaces containing shapes of mountain ridges and valley floors as shown in Fig. 1(a). We emphasize that both surfaces show the similar structure with narrow mountain ridges and broad valley floors. Figures 1(b) and 1(c) show the optical microscope images of the top surface after chemical etching of ~1.4 and 7 μm, respectively. These images demonstrate that a type-II pattern with narrow downward polarization domains near the top surface evolves into a type-I pattern with increasing depth: the ridges of the mountains in Fig. 1(a) reflect the narrow downward polarization domains near the top surface, and the valley floors in Fig. 1(a) exhibit the upward polarization domains inside of EMO-A (see also the Supplementary Information section 2 and 3). The corresponding schematics of ferroelectric domain configurations and their evolution are displayed in Figs. 1(d)-1(f). (Figures 1(d) and 1(f) are the schematics of Figs. 1(b) and 1(c), respectively. Figure 1(e) is drawn from the mid-height contour plot of Fig. 1(a).) As demonstrated in Fig. 1(d), the ferroelectric domain patterns near the original surfaces are type-II, but the patterns are type-I inside of the crystal as Fig. 1(f) shows.

Graph theory is useful to understand the seemingly-irregular patterns of ferroelectric domains in hexagonal $REMnO_3$ [17]. For example, figure 1(f) can be considered as a 6-valent graph where each domain, (even-gon), is surrounded by even number of vortices/antivortices, and six domain walls always merge at each vortex/antivortex core. This type-I pattern is $Z_2 \times Z_3$ colorable (see the Supplementary Information section 4) in the sense that all domains can be colored with 2 (dark and light) × 3 (red, blue, green) colors in a way that adjacent domains are colored in different colors (proper-colorable), and, for example, a dark red domain is never surrounded by light red domains. These dark and light colors correspond to upward and downward polarizations. On the other hand, figure 1(d) can be considered as a 3-valent graph where all domains with one of dark or light colors are always two-gons. When these two-gons are considered as lines (or edges), then the 6-valent graph with even-gons can be compactified as a “3-valent graph with even-gons”, which is 3-proper-colorable. These 3 colors (red, blue and green) correspond to the 3 structural antiphases.

The physical meaning of this $Z_2 \times Z_3$ coloring is that all domains of any ferroelectric domain pattern forming a 6-valent graph with even-gons can be assigned with α+, α–, β+, β–, γ+, and γ– in the way that, for example, an α+ domain is surrounded only by β– and γ– domains. The type-I patterns exhibit $Z_2 \times Z_3$ symmetry in the sense that the topology of the patterns remains intact with respect to the exchange of (+,-) or (α, β, γ) indices, and the symmetry between + and – is broken in the type-II patterns. In other words, the type-II patterns, which can be considered as 3-valent graphs with even-gons after compactification, show only Z_3-symmetry with broken Z_2-symmetry. All color schemes in the schematics of Figs. 1(d)-1(f) are consistent with the $Z_2 \times Z_3$ coloring. Note that this symmetry approach for domain patterns, regardless of relevant order parameters and microscopic Hamiltonian, reveals the macroscopic topological configuration of the interlocked domains with structural antiphase and ferroelectric polarization.

Interesting systematics emerge when the $Z_2 \times Z_3$ colors in the schematics of Figs. 1(d) and 1(f) are compared. First, the switching from Fig. 1(f) to Fig. 1(d) through Fig. 1(e) can be considered as a topological condensation through the breaking of the Z_2-symmetry in the sense that all dark downward polarization domains become two-gons, with each two-gon connecting one vortex and one antivortex. Then, one can consider the opposite process as topological evaporation through the restoration of Z_2-symmetry. (See the Supplementary Information section 2 for topological anti-condensation and anti-evaporation.) We note that during topological (anti-)condensation and (anti-)evaporation, most of the cores of vortices and antivortices are hardly influenced since their locations are nearly fixed. Nevertheless, we have observed the appearance of vortex-antivortex pairs with the low generation rate of less than one pair per 4.2×10^{-4} μm^{-2}, which are discussed in the Supplementary Information section 5.

Investigation by high-resolution TEM confirms that the structural antiphase relationship across one narrow domain is consistent with the $Z_2 \times Z_3$ coloring; i.e., one structural antiphase domain is surrounded by domains with two other structural antiphases. Figure 2(a) shows the optical microscope image of a type-II vortex-antivortex domain on the surface of the etched EMO-B sample. The dark line in the cross-sectional dark-field TEM image of the light-blue region in Fig. 2(a), shown in the inset of Fig. 2(a), corresponds to the narrow upward polarization domain. The dark contrast in the dark-field TEM image originates from breaking of a Friedel's pair in ferroelectrics, and thus confirms that the narrow domain has a ferroelectric polarization opposite to those of its two neighboring domains. Figure 2(b) displays a high-resolution TEM image and the inverse-fast-Fourier-transform (IFFT) image of neighboring domains. Domain boundaries are shown with hatched yellow lines. The broadening of the boundaries may result from the tilting of the boundaries along the depth direction. The solid sinusoidal curves in Fig. 2(c) are intensity scans of the blue and red rectangular areas in the IFFT image of Fig. 2(b), and also extrapolated from the solid curves to check the phase shift between structural antiphases. It should be noted that the modulation in the IFFT image of $\beta+$ could be an artifact due to the interference between the phase components in $\alpha-$ and $\gamma-$ domains. The periodic sinusoidal curves reflect the superlattice modulations due to the Er distortions along the c axis and the tilting of MnO_5 hexahedra in $ErMnO_3$. The presence of the phase shift between the two curves demonstrates that two – ferroelectric domains neighboring the narrow + ferroelectric domain have different structural antiphases. This observation, combined with the fact that structural antiphase domain walls are mutually interlocked with ferroelectric domains, does confirm that all neighboring three domains do have different structural antiphases [13].

The topological evolution of a domain pattern with Z_2-symmtry breaking with little change of the overall vortex-core structure is primarily associated with the local interaction between the partial dislocations (i.e., the structural antiphase/ferroelectric domain walls), but not with the interaction between vortices and antivortiecs. As shown in Figs. 3(a) and 3(b), the [α–, β+] structural antiphase wall can be considered as a partial dislocation with the Burgers vector of (+, 2π/3), where 2π/3 denotes the phase shift between two structural antiphase domains and + represents the change in polarization direction from – to +. In the same manner, the [β+, γ–], [γ–, β+], and [β+, α–] walls can be considered as partial dislocations with the Burgers vectors of (–, 2π/3), (+,–2π/3), and (–,–2π/3), respectively. If the [α–, β+] and [β+, γ–] walls with the same sign of the Burgers vectors merge, then the resultant wall would be coupled with the Burgers vector of (0, 4π/3), associated with a structural antiphase shift of 4π/3 without changing polarization direction. However, we did not observe any structural antiphase shift without changing polarization direction in our TEM results. This experimental finding, combined with the presence of $Z_2 \times Z_3$ coloring indicates that any wall with the Burgers vector of (0, 4π/3) does not exist. On the other hand, when the [α–, β+] and [β+, α–] walls with Burgers vectors with the opposite sign merge, the Burgers vector becomes zero, i.e., the resultant wall disappears. These results are consistent with the general behavior that two dislocations (or anti-dislocations) with the same Burgers vector tend to be repulsive to each other, whereas a pair of a dislocation and an anti-dislocation with the opposite Burgers vectors can exhibit an attractive interaction [18].

The repulsive interaction between partial dislocations appears responsible for the distribution of wall angles at vortex cores, where partial dislocations of [α–, β+], [β+, γ–], [γ–, α+], [α+, β–], [β–, γ+], and [γ+,α–] meet. As shown in Fig. 3(c), the median of the wall angle distribution of a type-I pattern is slightly below 60° degree. In contrast, the "random" distribution of six different angles should be monotonic as shown in the Supplementary Information section 6. Near vortex cores where partial dislocation walls are proximate to each other, the repulsive interaction between adjacent partial dislocations results in the depression of low angle density with a median value close to 60° in the distribution of six different angles. Note that the average value of the wall angle in our case as well as the random case is ~60°, as expected.

The interactions among partial dislocations and anti-dislocations play an essential role in the processes of topological (anti-)condensation and (anti-)evaporation. In general, the planar structure of partial (anti-)dislocations is associated with a 1/r-type distance dependence of mutual interaction [8, 18]. For example, the partial dislocation pair of [α–, β+] and [β+, γ–] walls with the same Burgers vector can have 1/r-type repulsive interaction. In the presence of electric fields (or effective electric fields in the case of self-poling), favoring – domains, the pair can be stabilized at a short distance where the total potential is minimal. This stabilization appears to be responsible for the presence of narrow domains in the type-II patterns. On the other hand, the partial dislocation-antidislocation pair of [α–, β+] and [β+, α–] walls with the opposite Burgers vectors can have attractive interaction, and be eventually mutually annihilated. Note that a recent electronic structure calculation reported a negligible interaction between domain walls [19]. Further investigation of the interaction is highly needed, considering that self-poling results in the finite width of narrow domains in the type-II domain patterns, which is a hallmark for the existence of a short-range repulsive interaction between partial dislocation pairs, as further discussed below.

This local interaction between partial dislocations governs the macroscopic behaviors of topological $Z_2 \times Z_3$ symmetry and Z_2-symmetry breaking. As shown in Fig. 4, the height profile of the AFM image of the middle region of the white-dashed-line rectangle in Fig. 1(b) demonstrates this annihilation process through topological evaporation. First, the narrow two-gon domains in Fig. 1(b) are due to the stabilization of repulsive partial (anti-)dislocation pairs. The topological evaporation process can be visualized from the evolution of red dashed lines from Figs. 4(b) to 4(f), which plot the equal height contour lines of the AFM image. Recall that narrow domains in EMO-A for Fig. 1, unlike EMO-B, are associated with – polarization. Basically, through topological evaporation, α– domains enlarge from narrow two-gons, and the partial dislocation-antidislocation pair of [α–, β+] and [β+, α–] walls can be eventually annihilated, so the β+ domain disappears and the α– domain becomes significantly extended. A similar annihilation process occurs for the partial dislocation-antidislocation pair of [α–, γ+] and [γ+, α–] walls in Fig. 4. In the processes of topological condensation and evaporation shown in Fig. 4, the creation and annihilation of partial dislocation pairs, probably associated with their mutual interaction, are responsible locally for the overall topology change between the type-I and type-II domain patterns.

In summary, we found that the $Z_2 \times Z_3$ symmetry emerges in the seemingly irregular ferroelectric domain patterns of $ErMnO_3$. Poling or self-poling processes induce topological transitions of ferroelectric domains through topological condensation and evaporation. These transitions are associated with the breaking and restoring of the Z_2 part of the $Z_2 \times Z_3$ symmetry. The creation and annihilation of pairs of partial dislocations and anti-dislocations with opposite Burgers vectors, i.e., the ferroelectric domain walls interlocked with structural antiphase, and the short-range repulsive interaction between dislocation (or anti-dislocation) pairs are locally responsible for the topological transitions.

Acknowledgements

We thank P. Leath for critical reading of the manuscript. This work was supported by National Science Foundation DMR-1104484.

References

[1] J. E. Scheib, S. W. Gangestad, and R. Thornhill, Proc. R. Soc. London Ser. B **266**, 1913 (1999).

[2] D. B. Lichtenberg, *Unitary symmetry and elementary particles* (Academic Press, Inc., New York, 1978).

[3] J. P. Hirth, and J. Lothe, *Theory of dislocations* (John Wiley and Sons, Inc., New York, 1982).

[4] M. A. Meyers, A. Mishra, and D. J. Benson, Prog. Mater. Sci. **51**, 427 (2006).

[5] C. H. Chen, J. M. Gibson, and R. M. Fleming, Phys. Rev. Lett. **47**, 723 (1981).

[6] M. B. Walker, Phys. Rev. B **26**, 6208 (1982).

[7] K. K. Fung, S. McKernan, J. W. Steeds, and J. A. Wilson, J. Phys. C **14**, 5417 (1981).

[8] H. J. Schulz, B. I. Halperin, and C. L. Henley, Phys. Rev. B **26**, 3797 (1982).

[9] C. J. Fennie, and K. M. Rabe, Phys. Rev. B **72**, 100103 (2005).

[10] B. B. Van Aken, T. T. M. Palstra, A. Filippetti, and N. A. Spaldin, Nature Mater. **3**, 164 (2004).

[11] T. Lonkai, D. G. Tomuta, U. Amann, J. Ihringer, R. W. A. Hendrikx, ouml, D. M. bbens, and J. A. Mydosh, Phys. Rev. B **69**, 134108 (2004).

[12] A. S. Gibbs, K. S. Knight, and P. Lightfoot, Phys. Rev. B **83**, 094111 (2011).

[13] T. Katsufuji, S. Mori, M. Masaki, Y. Moritomo, N. Yamamoto, and H. Takagi, Phys. Rev. B **64**, 104419 (2001).

[14] Q. Zhang, L. Wang, X. Wei, R. Yu, L. Gu, A. Hirata, M. Chen, C. Jin, Y. Yao, and Y. Wang, Phys. Rev. B **85**, 20102 (2012).

[15] T. Choi, Y. Horibe, H. T. Yi, Y. J. Choi, W. Wu, and S. W. Cheong, Nature Mater. **9**, 253 (2010).

[16] T. Jungk, A. Hoffmann, M. Fiebig, and E. Soergel, Appl. Phys. Lett. **97**, 012904 (2010).

[17] S. C. Chae, Y. Horibe, D. Y. Jeong, S. Rodan, N. Lee, and S. W. Cheong, Proc. Natl. Acad. Sci. U. S. A. **107**, 21366 (2010).

[18] A. N. Stroh, Philos. Mag. **3**, 625 (1958).

[19] Y. Kumagai, and N. A. Spaldin, arXiv preprint arXiv:1207.4080 (2012).

Figure legends

FIG. 1 (color online) Depth profiles using sequential chemical etching and $Z_2 \times Z_3$ coloring. (a) Three- dimensional atomic force microscope (AFM) image of the top (001) surface of the EMO-A sample after 7 μm chemical etching. (b) and (c) Optical microscope images of the top (001) surface of EMO-A after 1.4 and 7 μm chemical etching, respectively. Dashed rectangles in Figs. 1(b) and 1(c) correspond to the AFM scanned region of Fig. 1(a). (d) and (f) Schematics of the white-dashed-line rectangle region in Figs.1(b) and 1(c) with $Z_2 \times Z_3$ coloring, respectively. (e) Schematic of an intermediate domain pattern between Figs. 1(d) and 1(f). The depth was estimated from the mid height contour plot of Fig. 1(a).

FIG. 2 (color online) (a) Planar optical microscope image of the type-II pattern of EMO-B after chemical etching. The inset shows a cross-sectional TEM image of the purple-line region. (b) High-resolution TEM image of the orange rectangle region in the inset of Fig. 2(a). (c) The structural antiphase shift between α– and γ– phases for the red and blue rectangles in Fig. 2(b), respectively. Red and blue sinusoidal waves indicate the periodicity of atoms in the red and blue rectangles, respectively.

FIG. 3 (color online) (a) and (b) The local lattice distortions near the α–/β+/γ– and α–/β+/α– domain boundaries in hexagonal $RMnO_3$, respectively. The yellow, brown, and blue circles represent the Y, Mn, and O ions, respectively. The light blue and dark blue circles indicate the top and bottom apical oxygen ions of MnO_5 hexahedra. The arrows depict the directions of atomic distortions. The triangles with green bars correspond to Mn trimers. (c) The experimental distribution of the relative angle between adjacent partial dislocations near vortex cores. The red dashed line is drawn as a guide for eyes. The inset shows an AFM image with the definition of the angle (θ) between two adjacent domain boundaries. The dashed black line indicates the average value of 60°, and the arrow indicates the median (~55°) of the angle distribution.

FIG. 4 (color online) Topological evaporation from type-II to type-I. (a) AFM image of the middle region of the white-dashed-line rectangle in Fig. 1(c). (b)–(f) Schematics of evolution from type-II to type-I patterns with attractive interaction and eventual annihilation of partial dislocation-antidislocation pairs ([α–, β+]-[β+, α–] walls and [α–, γ+]-[γ+, α–] walls).

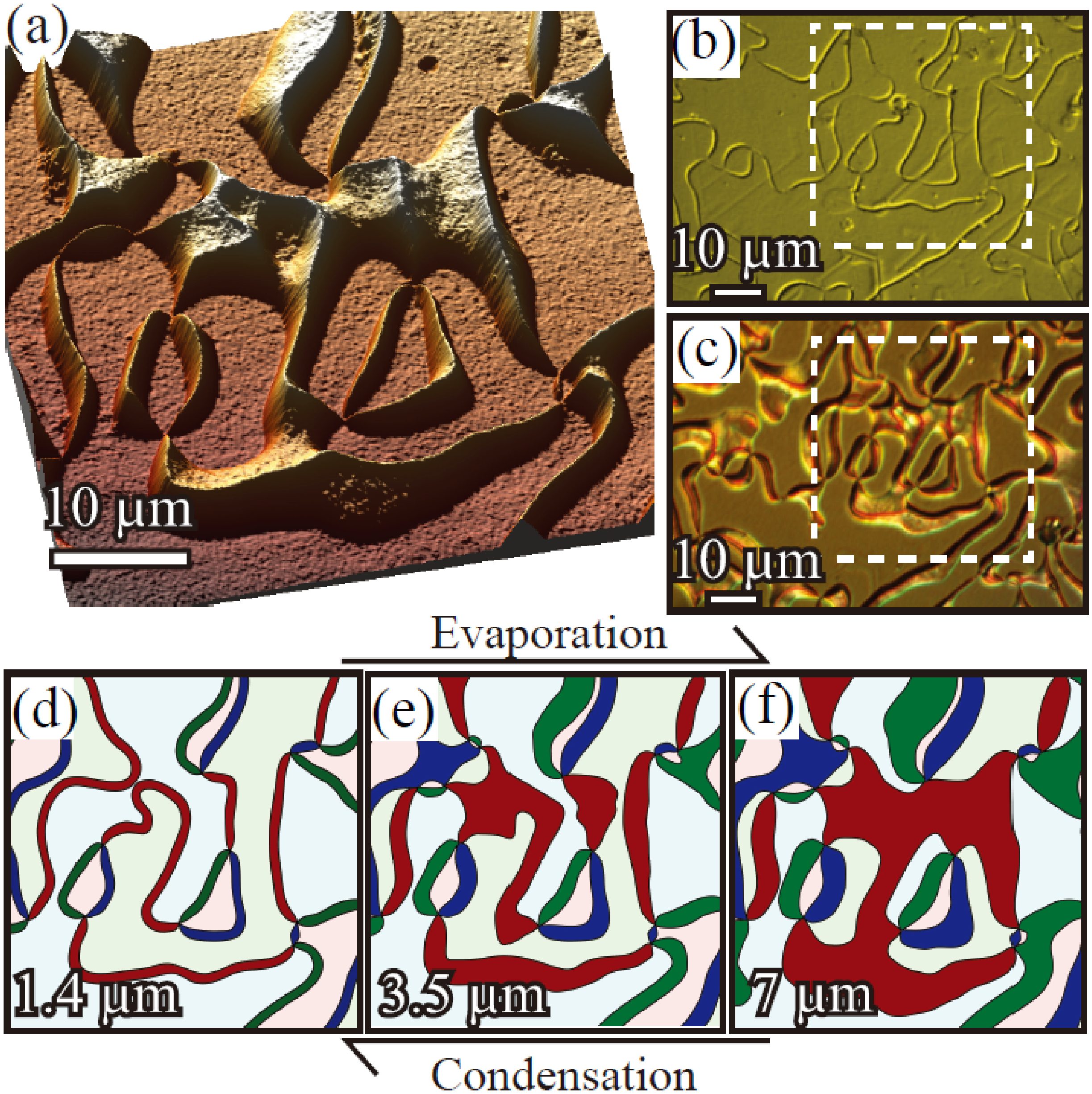
(a)
10 μm
(b)
10 μm
(c)
10 μm
Evaporation
(d)
1.4 μm
(e)
3.5 μm
(f)
7 μm
Condensation

Figure 1

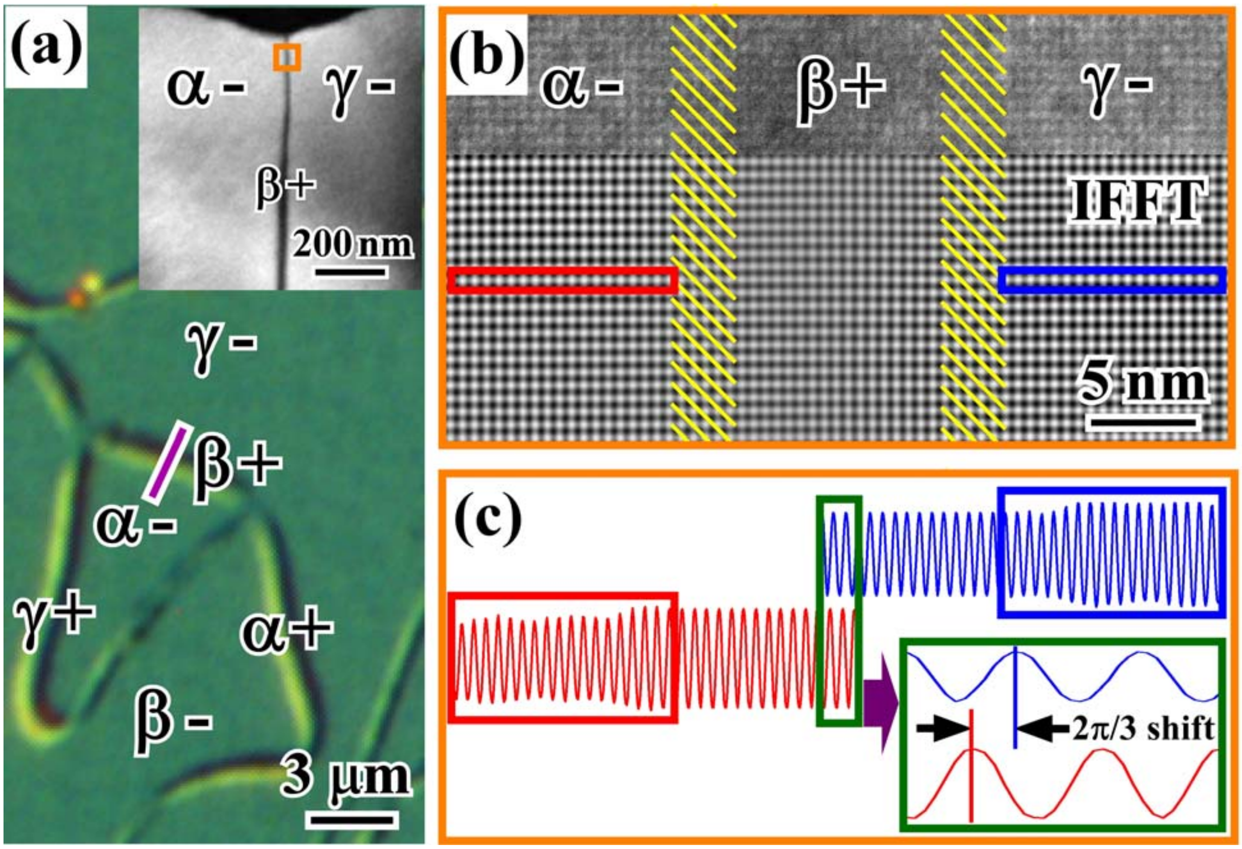

Figure 2

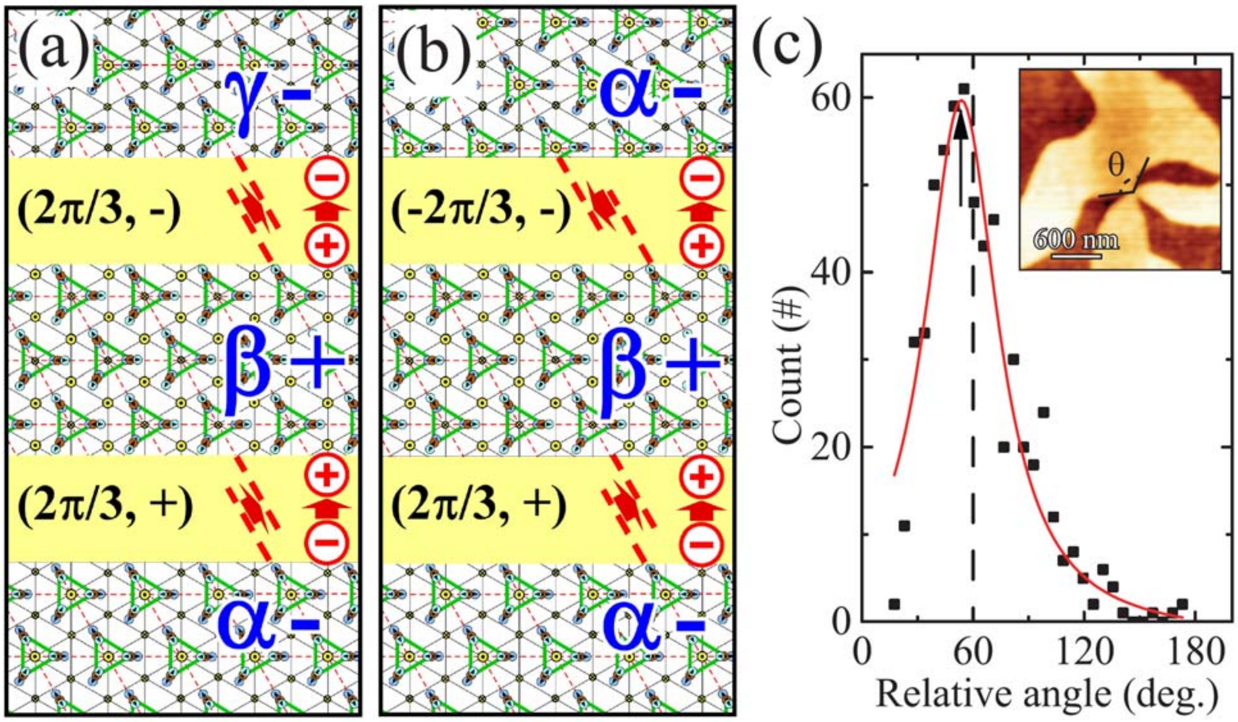
(a)
γ-
(2π/3, -)
β+
(2π/3, +)
α-
(b)
α-
(-2π/3, -)
β+
(2π/3, +)
α-
(c)
θ
600 nm
Count (#)
0
20
40
60
0
60
120
180
Relative angle (deg.)

Figure 3

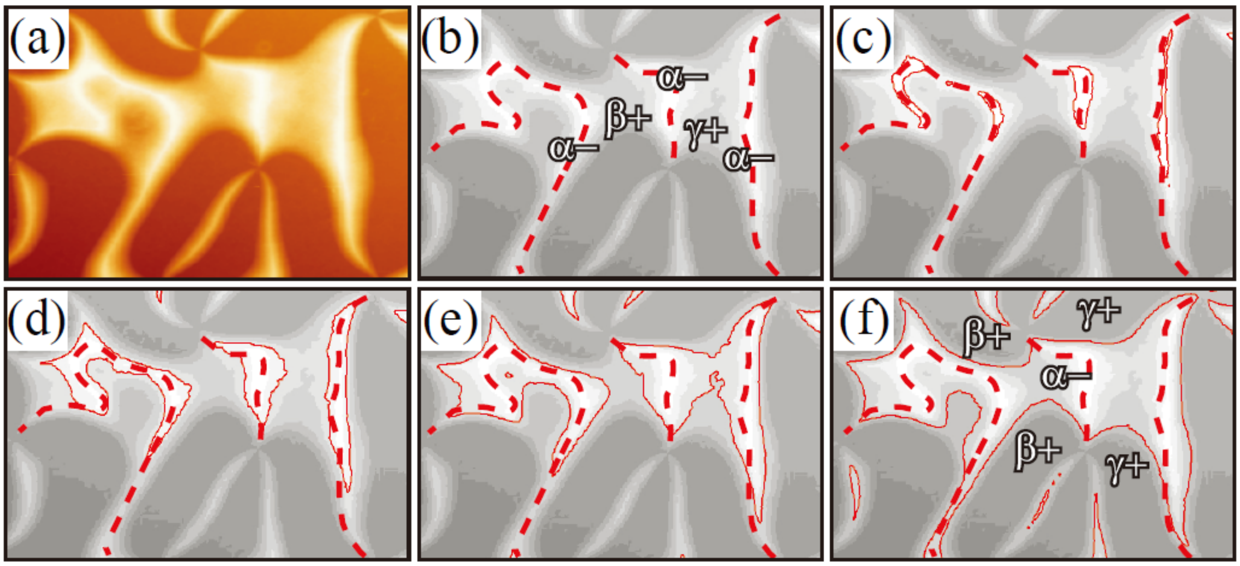

Figure 4